



# Predicting the overall response of an orthogonal 3D woven composite using simulated and tomography-derived geometry



Adam Ewert<sup>a</sup>, Borys Drach<sup>a,\*</sup>, Kostiantyn Vasylevskyi<sup>b</sup>, Igor Tsukrov<sup>b</sup>

<sup>a</sup> Mechanical & Aerospace Engineering, New Mexico State University, Las Cruces, NM, United States

<sup>b</sup> Mechanical Engineering, University of New Hampshire, Durham, NH, United States

## ABSTRACT

Effects of two *meso*-scale geometry generation approaches on predicting effective elastic properties and thermal conductivity of an orthogonal 3D woven composite are studied in this paper. The two approaches used are fabric mechanics simulation (DFMA software, Kansas State University) and direct processing of X-ray microtomography ( $\mu$ CT) data. Two models are created in DFMA using two different sets of cross-sectional areas as input: nominal (based on the initial weave pattern) and adjusted (informed by volume fraction measurements obtained from microscopy data). In addition, one conformal mesh and three voxel mesh models are created from  $\mu$ CT data. Experimental measurements of transverse Young's moduli are used to evaluate the accuracy of the predicted results.

In each case, a unit cell with in-plane periodic boundary conditions is modeled, which has not been previously done in the case of  $\mu$ CT-based models. The effect of high frequency oscillations in local material orientations imparted by a wavy centerline (artifact of  $\mu$ CT image processing) on the elastic and thermal conductivity properties is studied. The differences in volume fractions and shapes of bundles of fibers (tows) between  $\mu$ CT-based and DFMA-based models are also investigated to determine sensitivity of effective thermo-mechanical properties to each of these factors.

## 1. Introduction

Advantages offered by 3D woven composite materials (e.g. high delamination resistance, good impact resistance, and dimensional stability) have led to their increasing use in the aerospace and other performance driven industries [1]. As the demand for 3D woven composites increases, understanding how their design affects elastic and thermal properties becomes more important for creating better and safer composites.

Exploring new composite designs experimentally is both time consuming and expensive. Moreover, measuring some properties like out of plane Young's and shear moduli can be hard if not impossible, creating the need for predictive modeling. Some analytical approaches may work well for predicting the overall material properties of 2D woven composites [2]. However, these approaches are often inadequate for 3D woven architectures [3]. This motivates interest in quantifying the effects of *meso*-scale features on predictions of effective elastic and thermal properties which can be studied using high fidelity finite element analysis (FEA). Studying these effects on the macro-scale level is challenging due to computational constraints. The alternative approach is to analyze a single unit cell (UC) of a woven composite at the *meso*-scale.

Several different methods exist to create the UC geometry representation for virtual testing. The easiest way to create geometry is by

describing the nominal weave pattern using homogenized bundles of fibers (tows) with a constant cross section (see, for example, [4,5]). This method does not capture the localized tow deformations inherent in the manufacturing process and often does not match the experimentally measured volume fraction of fibers [6]. The digital element method (DE) has been developed to capture tow deformations due to weaving. DE-based models allow for better characterization of resulting tow shape from the weaving process by simulating multiple threads per tow and their interactions [7–9]. As tension is applied to fiber bundles, the tows interact and their cross sections are subjected to non-uniform transverse deformation. This method often leads to overlapping of tow geometries, which must be corrected before analysis can be performed.

Alternatively, 3D woven geometry can be obtained from X-ray microtomography ( $\mu$ CT) or serial sectioning using optical microscopy of an existing specimen to capture a volumetric point cloud representing the reinforcement. The point cloud is constructed from multiple images, each representing a slice of the material. X-ray microtomography images of carbon/epoxy composites are notoriously noisy and have low contrast between the tows and the matrix due to similar absorption properties of the materials [10]. Because of the noise, the images are difficult to process via automated segmentation techniques, requiring manual intervention. However, once created,  $\mu$ CT-based models are the most accurate virtual representations of a composite material as they are reconstructed from actual specimens [10]. This makes them

\* Corresponding author at: Borys Drach, Mechanical and Aerospace Engineering, New Mexico State University, P.O. Box 30001, MSC 3450, Las Cruces, NM 88003-8001, United States.

E-mail address: [borys@nmsu.edu](mailto:borys@nmsu.edu) (B. Drach).

<https://doi.org/10.1016/j.compstruct.2020.112169>

Received 28 October 2019; Received in revised form 24 January 2020; Accepted 10 March 2020

Available online 13 March 2020

0263-8223/ © 2020 Elsevier Ltd. All rights reserved.

especially valuable for calibration of other geometry generation techniques.

A review by Ansar et al. [11] finds that nominal tow geometry is able to characterize the volume fraction well in non-orthogonally woven architectures. A study by Lee et al. [12] compares an idealized orthogonal model to experimental results. While achieving good correlation in the final model's predictions with experimental data, the study uses numerical corrections to account for crimping and waviness instead of using actual geometry. Multiple unit cells of repeating geometry are used, which leads to a high computational cost when studying tow and matrix interaction. To improve the ideal textile model, Green et al. [13] introduces a numerical model to predict deformations caused by weaving and compaction and incorporate the changes into the mesh. The deformation model takes into account average tow waviness and implements correction using a convex hull algorithm. However, to match experimental results for ultimate tensile strength within 1%, the fiber volume fraction for the augmented mesh has to be reduced by 6.5% from the measured value. Comparing the ideal model to the deformed model, Green et al. find that ideal geometry is not adequate for representing textiles with complex internal architecture, though only in-plane elastic moduli are considered. Liu et al. [14] compares microtomography-based geometry to ideal geometry of an orthogonal glass composite finding significant over-prediction by the idealized model in the warp direction. While periodic boundary conditions are used for the ideal model, kinematic uniform boundary conditions are used for the microtomography-based model. Joglekar et al. [15] employs a conformal mesh based on the DE method to fully simulate the weave process and to study compaction effects. They report the simulated geometry dimensions within 5% of experimental measurements. Timoshchuk et al. [16] finds good correlation with tomography data when predicting locations of potential damage as a result of residual stresses developed due to cooling from cure to room temperature. Drach et al. [17] uses a conformal mesh based on the DE simulations to determine effective elastic properties as well as thermo-elastic properties. Other authors interested in conductive properties of 3D woven composites have mainly focused on conductivity in the through-thickness direction [18–20].

While there are many studies concerning the prediction of elastic and thermal conductivity properties of 3D woven fabrics, most of them simplify *meso*-scale geometry for ease of homogenization. Comparative studies, e.g. Liu et al. [14], do not always use consistent boundary conditions to compare models. To our knowledge, direct comparison between the simulated tow mesh based on weave process simulations,  $\mu$ CT-based voxel and conformal meshes, and experimental data has not been performed. Each model studied in this paper employs periodic boundary conditions over a single representative UC, which has not been previously done in the case of  $\mu$ CT-based meshes. The goal of this study is to determine the effect the *meso*-scale geometry generation

approaches have on predicting effective elastic and thermal conductivity properties using FEA. Note that there might be other potential sources of variability in woven composites including material properties of the constituents, variations of fiber volume fractions inside the tows and tow misplacement; however, these sources are considered outside of the scope of this paper.

In all analyses presented here, geometric modeling is informed by the same high resolution imaging data of a single unit cell. Experimental results obtained by Vyshenska [21] ranging from 72.3 GPa to 84.12 GPa in the warp direction and from 60.8 GPa to 70.78 GPa in the weft direction are used to evaluate the accuracy of the predictions made by FEA. The average values for each range, 77.3 GPa in the warp and 65.8 GPa in the weft directions, are used for comparison.

The paper is organized as follows. Section 2 discusses the methodology of geometry generation using a simulated weaving approach, and mesh generation based on X-ray microtomography. Then the differences in the geometries are compared. A discussion on voxel meshes compared to conformal meshes concludes Section 2. Section 3 provides material properties used and details periodic boundary conditions as well as methodology for determining the effective elastic and thermal conductivity properties. Section 4 presents simulation results including the effect of material orientations on the effective elastic properties, comparison of DFMA-simulated with  $\mu$ CT-based models, and discussion of differences between voxel and conformal meshes. Concluding remarks are given in Section 5.

## 2. Geometry and mesh preparation methodology

### 2.1. Digital fabric mechanics approach

Two of the orthogonal meshes used in this paper are generated using DFMA (abbreviation of Digital Fabric Mechanics Analyzer), a digital element method software developed at Kansas State University [7]. This and similar dry fiber fabric mechanics simulation methods have been used in the community to generate “as-woven” reinforcement geometries, see, for example, [15] and [22]. In the approach, characteristics of a UC such as the number of warp and weft layers, weave pattern, and cross-sectional area of the tows are used as inputs to begin the modeling process. The initial pattern of individual tows represented as cylinders, as shown in Fig. 1a, is generated by the software. The tows are then subdivided into bundles of digital elements subjected to tensile forces, which results in contact interaction of these elements creating non-uniform cross sections, see Fig. 1b. Using this process, two models were created for our analysis. Expected areas of tow cross sections based on the number of fibers, fiber diameter, and fiber volume fraction in each tow were used in the first model, “DFMA-1”. As will be shown below, this model's tow volume fractions of the warp and weft tow groups do

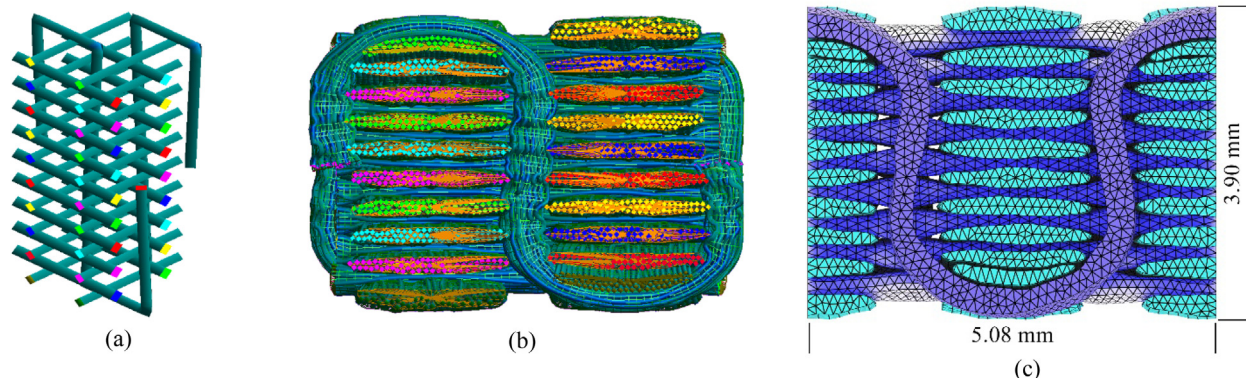


Fig. 1. Abbreviated DFMA workflow showing the “DFMA-2” model: (a) initial weave pattern represented by cylindrical tows; (b) tows represented by bundles of digital element chains; (c) FEA-ready volumetric mesh of the composite unit cell (matrix mesh is hidden).

not match the experimentally measured microtomography results. The second model, “DFMA-2”, addresses this issue by using adjusted cross-sectional areas that lead to tow volume fractions that more closely match the  $\mu$ CT measurements.

The final deformed fabric is exported from DFMA as a point cloud and further processed to create an FEA ready mesh. The end caps of the mesh generated from the DFMA point cloud are not parallel to the boundaries of the UC and it is common for the tows to have interpenetrations. A custom Matlab script detects the interpenetrating elements, then moves them along the normal until the elements no longer overlap. This results in a mesh where each tow is isolated and does not touch any other tow. End caps are made flat by taking advantage of the periodic nature of the unit cell each – tow is extended beyond the UC boundary and then cut to the correct length. To avoid narrow longitudinal sections of the tows being isolated when cutting, the UC is shifted to split binder and weft tows down the middle (compare Fig. 1b and c). For details on the original DFMA geometry preparation process see [23].

It was noticed that in the model generated using the unmodified DFMA process, the weft tows’ volume fraction is higher than the warp tows’ volume fraction which is opposite to the measured values, compare volume fractions of “DFMA-1” with “ $\mu$ CT-Co” ( $\mu$ CT-based model) in Table 1. For the second DFMA implementation, the process was slightly modified to match the volume fraction seen in the manufactured physical specimen. The volume fractions were altered by changing the input cross-sectional area. Due to the unstable nature of the relaxation process, there is no strong correlation between the input cross-sectional area and the output volume fraction. In addition, the interpenetration fixing step is observed to reduce the warp and weft volume fractions by approximately 13% and the binder volume by 4%. Thus, to generate the final “DFMA-2” model, the input cross section areas were updated iteratively until the volume fractions of the warp, weft and binder tow groups were within 2% of the  $\mu$ CT data, compare columns “DFMA-2” and “ $\mu$ CT-Co” in Table 1.

After checking for periodicity in the surface mesh, each model is meshed with volumetric tetrahedral four-node (tet-4) elements. Tow center points are used to create an orientation for each element with the primary direction pointing along the tow direction. Once material orientations are assigned, the volume elements are converted to tetrahedral ten-node (tet-10) elements. The final “DFMA-1” model contains 788,182 nodes and 558,587 elements, and the “DFMA-2” model contains 921,517 nodes and 672,872 elements.

To ensure mesh independence of the FEA predictions, we remeshed DFMA-2 model with 1.6 million elements and compared the predicted effective thermo-elastic properties. The difference in predictions was within 1%. This shows that for the microstructures considered in this paper, FEA meshes with approximately 600 k of ten-node tetrahedral elements are sufficiently dense for the effective property calculations.

## 2.2. Microtomography approach

X-ray microtomography data for one unit cell of a carbon/epoxy composite with one-to-one orthogonal reinforcement architecture was

**Table 1**

Volume fractions of different tow groups in simulated (“DFMA”) and microtomography-based (“ $\mu$ CT”) meshes, %. Volume fractions for conformal (“Co”) and voxel (“VX”) meshes having three resolutions (75, 100 and 125 voxels in the thickness direction) are given.

	DFMA-1	DFMA-2	$\mu$ CT-Co	$\mu$ CT-VX_75	$\mu$ CT-VX_100	$\mu$ CT-VX_125
$V_{fwarp}$	26.6	31.6	31.6	31.8	31.7	31.7
$V_{fweft}$	33.3	26.8	29.0	28.6	29.1	29.4
$V_{fbinder}$	8.42	7.37	6.76	6.60	6.70	6.80
$V_{ftotal}$	68.3	65.8	67.4	67.0	67.5	67.9

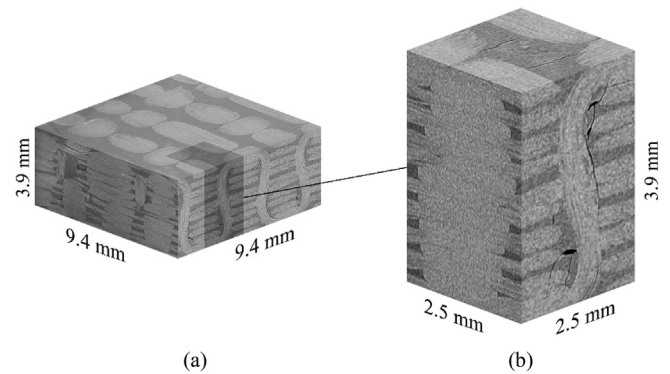


**Fig. 2.** Microtomography data: (a) full dataset and (b) section selected for tow geometry extraction.

provided by the manufacturer Albany Engineered Composites (Rochester, NH). The data (which has the resolution of  $7.5 \mu\text{m}$ ) was used to generate a conformal, “ $\mu$ CT-Co”, and three voxel meshes, “ $\mu$ CT-VX\_75”, “ $\mu$ CT-VX\_100” and “ $\mu$ CT-VX\_125”. While the  $\mu$ CT scan contains more than one complete unit cell, only a quarter of a unit cell could be confidently used, see Fig. 2. This is due to a misplaced binder tow in the dataset causing irregularities in a large portion of the data. The quarter unit cell was mirrored to create a full unit cell after further processing. As can be seen in Fig. 2b, the material has some cure-induced microcracks (shown as black regions) in the matrix and along the matrix-tow interfaces. These local defects studied in [17,24] are expected to have negligible contribution to the overall material response because almost all of the stress and heat flux are carried by the tows.

Segmentation of the selected portion of the  $\mu$ CT data required to separate the tows from the matrix was performed in ImageJ [25]. Contrast between the matrix and the tow materials is low and the data is very noisy, which prohibits an automated segmentation process. In particular, due to the noise, the thresholding produces artificial features not present in the actual material such as small holes inside tows, bumps and pits on tow surfaces, and disconnected regions around tows. In addition, there is no way to automatically separate touching tows. As such, tow profiles in every 16th image in the stack were manually traced which resulted in 40 profiles per full-length tow, then ImageJ was used to interpolate between the traced outlines. The outlines were then filled with a solid color in each  $\mu$ CT slice and separated from the data, see Fig. 3. The quality of the final segmentation was checked by “reslicing” the segmented dataset and observing the tows from three orthogonal views.

While tracing the tow profiles, a slight gap was intentionally left

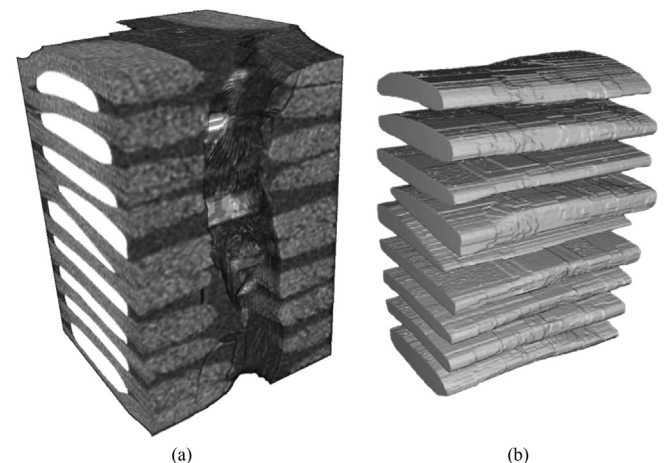


**Fig. 3.** Warp tows: (a) filled with a solid color as shown in the selected portion of the  $\mu$ CT data; (b) extracted surfaces.

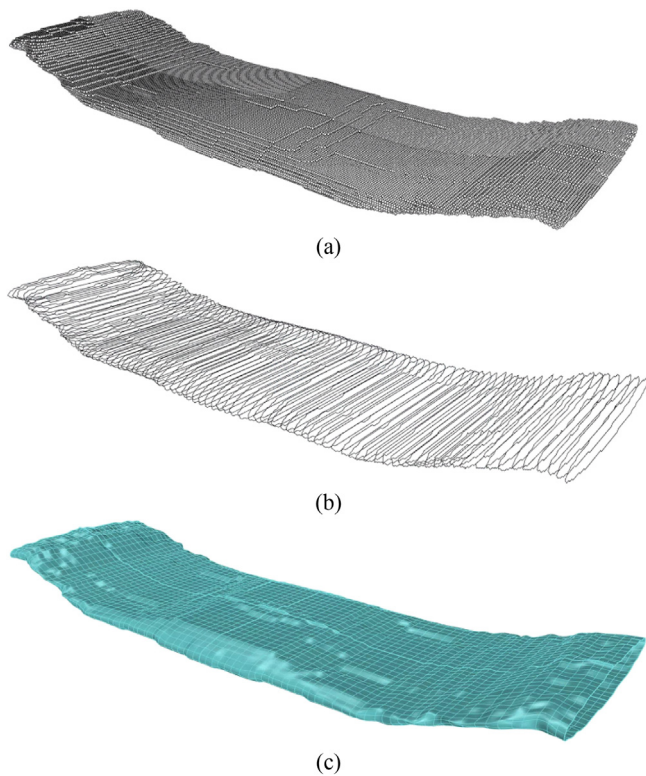


Fig. 4. Creating a NURBS surface: (a) point cloud; (b) splines created from the point cloud; (c) resulting NURBS surface.

between the tows that appeared to be touching. This was done because overlapping elements in the conformal mesh are not allowed [23]. With each tow isolated in this manner, a surface mesh was then generated and exported as an STL file. At this stage, the mesh needed to be trimmed to the correct size to match the periodic cell boundaries. Trimming the STL mesh directly would result in elements with poor aspect ratios. To avoid this and to create a smoother mesh, a non-uniform rational basis spline (NURBS, see [26] for mathematical formulation) surface was generated for each tow using vertices from the STL file, see Fig. 4.

After creating and trimming the NURBS surfaces to the correct size in Rhinoceros 3D modeling software [27], centerline points were created for later material orientation assignments. The quarter UC was then exported to MSC Patran for surface meshing. The meshed geometry was imported into MSC Mentat where the quarter UC was mirrored, creating the full periodic UC. This geometry was then made water tight and meshed with tet-4 vol elements. The empty space in the unit cell was meshed to generate the matrix volume. Following this, the centerline points generated in Rhinoceros software were used in a custom Python script to set material orientations for each tow element, resulting in the “Original  $\mu$ CT-Conformal” (“Original  $\mu$ CT-Co”) model. After orientations were assigned, tet-4 elements were converted to tet-10 elements. The final conformal microtomography-based mesh contains 843,378 nodes and 616,101 elements.

### 2.3. Comparison of tow geometries between DFMA- and $\mu$ CT-based meshes

While the DE method can simulate local tow deformations from the weaving process, there are still some effects, like compaction, that are not captured accurately, see Fig. 5. The  $\mu$ CT-based model is flatter on the top and bottom, where the top and bottom of the DFMA mesh are still rounded. Slight differences in the warp and weft tows can also be seen as there is more variation in shape in the  $\mu$ CT-based model.

In both DFMA models, excessive pinching can be seen in the warp

tows, see Fig. 6. As the warp tows are held under tension in the weaving process, this is not seen in the  $\mu$ CT mesh and may have an impact on the predicted effective elastic properties as discussed further in Section 4.2. In addition to flatter top and bottom, the binder tow takes on a more pronounced ‘S’ shape as the fabric is compacted. This effect is not captured at all in the “DFMA-1” model, but it is recreated in the “DFMA-2” model. It is expected that a straighter binder tow would artificially stiffen the through-thickness effective elastic properties as well as have an effect on thermal conductivity.

### 2.4. Voxel vs conformal meshing

In addition to conformal meshing, the  $\mu$ CT model is also meshed with “voxel” elements, see Fig. 7. A voxel mesh represents a structured grid of cubic elements having the same size. Structured grids are expected to be well-suited for effective property estimation, but not for accurate resolution of local stress and strain fields. Doitrand et al. [6] shows that a voxel mesh modeling a four-layer plain weave works well for predicting homogenized elastic properties.

Eight-node hexahedral elements are used in this study. The mesh is generated using a custom Matlab script as a MSC Marc Mentat input file. Matrix and tow elements are created at the same time. Different resolution levels are used to create three models. In these models, two adjacent tows may share nodes.

One of the main advantages of using structured grids is that the nodes on the opposite faces of a unit cell will always match. Special care needs to be taken to achieve the same when using conformal meshes. In addition, unlike in the case of conformal meshes, a gap between tows is not necessary in voxel meshes. As a result, mesh generation from  $\mu$ CT data can be easily automated. On the other hand, because all voxel are of the same size, capturing fine details in the tow geometry can result in models with too many degrees of freedom to be practically solved using a desktop computer.

A conformal tetrahedral mesh with variable element size can help capture fine detail and still be practical for solving. However, additional steps must be taken to ensure that meshes are congruent on the opposite faces of a unit cell. As a result, conformal meshes usually require a lot more manual intervention to set up as compared to voxel meshes.

## 3. Finite element analysis: model preparation and processing

### 3.1. Material properties

The FEA package MSC Marc Mentat [28] is used for analysis in this paper. The composite matrix is modeled as linearly elastic having the properties of the HEXCEL RTM6 epoxy resin with Young’s modulus  $E_m = 2.89 \text{ GPa}$ , Poisson’s ratio  $\nu_m = 0.35$  [29], and thermal conductivity  $k_m = 0.22 \frac{\text{W}}{\text{m} \cdot \text{K}}$  [30]. Each tow in the composite consists of 12,000 IM7 carbon fibers impregnated with RTM6 epoxy with fiber volume fraction of  $V_f = 80\%$  [23]. The tows are modeled as homogenized transversely isotropic solids with effective elastic properties calculated from Hashin’s homogenization expressions presented in [17,31,32] using manufacturer specified fiber properties [33]. Longitudinal thermal conductivity of a fiber is given by the manufacturer as  $k_{1f} = 5.4 \frac{\text{W}}{\text{m} \cdot \text{K}}$ , where subscript “1” denotes the longitudinal fiber direction. Transverse fiber conductivity is generally five times lower than longitudinal conductivity, giving a value of  $k_{2f} = 1.08 \frac{\text{W}}{\text{m} \cdot \text{K}}$  [18], where subscript “2” denotes the transverse fiber direction. According to Hashin [31], the rule of mixtures is acceptable for determining longitudinal thermal conductivity for a resin impregnated tow:

$$k_1 = V_f k_{1f} + (1 - V_f) k_m \quad (1)$$

Hashin also proposes the following expression for estimating the transverse thermal conductivity of a tow:

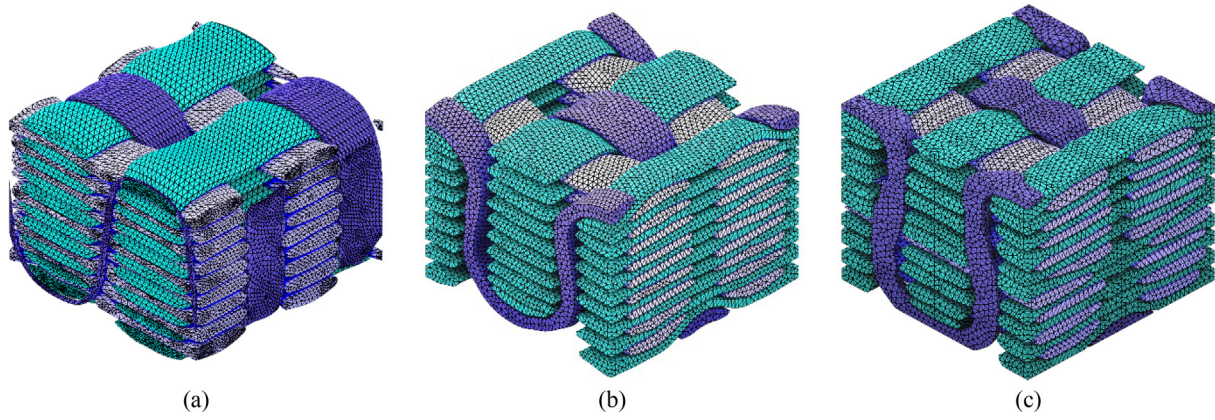


Fig. 5. Final reinforcement meshes: (a) conformal “DMFA-1”; (b) conformal “DMFA-2”; (c) conformal extracted from  $\mu$ CT data.

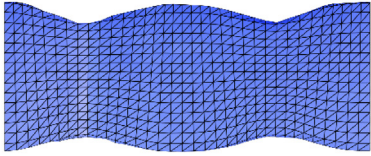
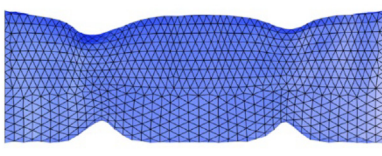
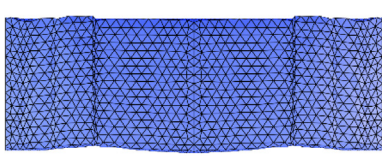
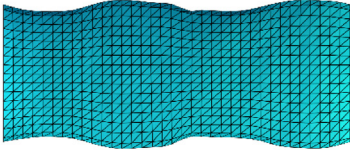
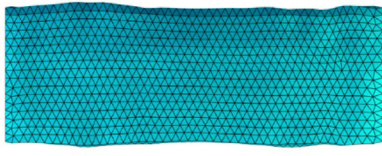
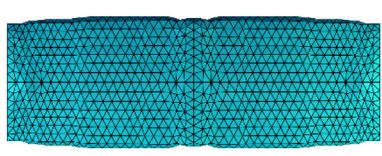
DFMA-1	DFMA-2	$\mu$ CT
		
Warp	Warp	Warp
		
Weft	Weft	Weft
		
Binder	Binder	Binder

Fig. 6. Comparison of tow shapes between the considered models.

$$k_2 = k_m \frac{k_m(1 - V_f) + k_{2f}(1 + V_f)}{k_m(1 + V_f) + k_{2f}(1 - V_f)} \quad (2)$$

Table 2 presents the elastic and thermal conductivity properties of IM7 fibers, and the effective elastic and thermal conductivity properties of resin impregnated tows used in the simulations.

### 3.2. Periodic boundary conditions

Periodic boundary conditions are applied in the warp and weft directions. The through-thickness dimension of the unit cell is assumed to represent the total thickness of a specimen and does not require

periodic boundary conditions to be applied. In periodic boundary conditions, displacements on unit cell faces are constrained by the following equation:

$$\mathbf{u}_{-i}^+ = \mathbf{u}_{-i}^- + \delta_{-i} \quad (i = \text{warp}, \text{weft}) \quad (3)$$

where  $\mathbf{u}_{-i}^+$  and  $\mathbf{u}_{-i}^-$  are the vectors of nodal displacements on the positive and negative faces of the unit cell, and  $\delta_{-i}$  is the vector of prescribed displacements in the  $i$ -th direction.

Similarly, thermal periodic boundary conditions are described by:

$$T_i^+ = T_i^- + \Delta_i \quad (i = \text{warp}, \text{weft}) \quad (4)$$

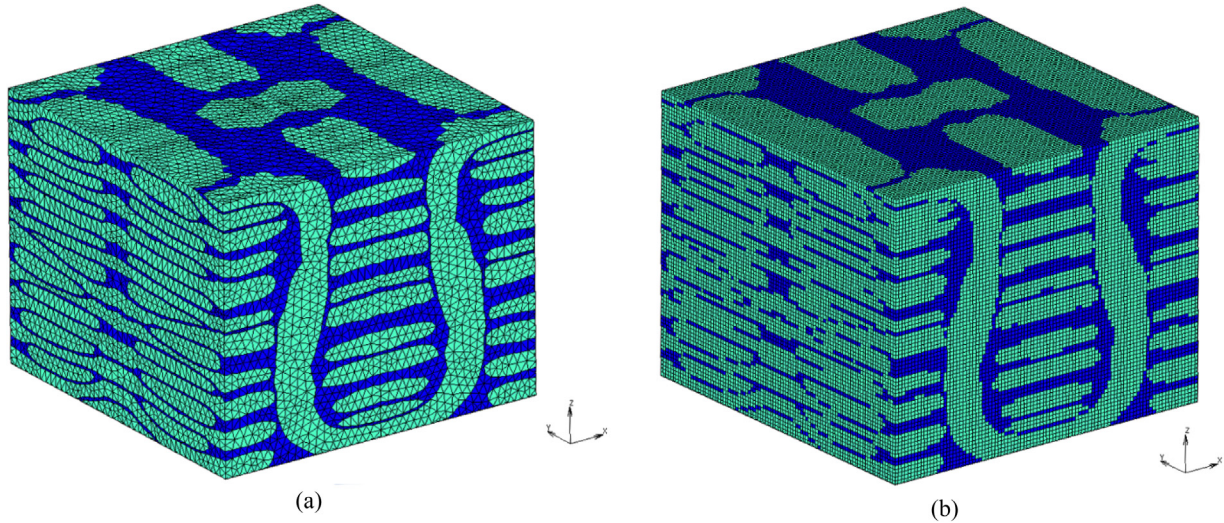


Fig. 7. Two mesh types used in this paper: (a) conformal tetrahedral mesh; (b) coarse voxel mesh (uniform hexahedral mesh with 75 elements across the unit cell thickness). Note higher resolution voxel meshes are not shown because individual elements are too small to resolve in the figures.

where  $T_i^+$  and  $T_i^-$  are the temperatures on the positive and negative faces, and  $\Delta_i$  is the change in temperature in the  $i$ -th direction. Using these conditions requires the opposing faces to have matching nodes as described in Section 2.1. This condition is automatically satisfied in a voxel mesh composed of uniform hexahedral elements.

### 3.3. Processing of simulation results

The orthogonal DFMA- and  $\mu$ CT-based models described in Section 2.2 are analyzed by subjecting them to uniaxial and shear mechanical loading to determine the effective elastic properties. The results are processed to relate the applied macroscopic strains with volume-averaged stresses, see [23]. Volume-averaged stress values are extracted for each load case using a custom Python script as follows:

$$\langle \sigma_{ij} \rangle_m = \frac{1}{V} \sum_{l=1}^{N_e} (\sigma_{ij}^{(l)})_m \cdot V^{(l)}, \quad i, j = 1, 2, 3 \quad (5)$$

where  $\langle \sigma_{ij} \rangle_m$  is the volume average of the stress component  $ij$  calculated from the  $m$ -th load case,  $V$  is the UC volume,  $(\sigma_{ij}^{(l)})_m$  is the stress component  $ij$  at the centroid of the finite element  $l$  calculated from the  $m$ -th load case,  $V^{(l)}$  is the volume of the element  $l$ , and  $N_e$  is the total number of elements in the model. The overall material stiffness components  $C_{ijkl}^{eff}$  are found as the proportionality coefficients relating macroscopic strains with volume-averaged stresses. For example, in the first load case (tension in the warp direction):  $C_{ijkl}^{eff} \cdot (\epsilon_{kl}^0)_1 = \langle \sigma_{ij} \rangle_1$  ( $i, j, k, l = 1, 2, 3$ ) there is only one non-zero component of applied strain  $(\epsilon_{11}^0)_1$  which can be used to obtain stiffness components  $C_{ij11}^{eff}$  [34]:

$$C_{ij11}^{eff} = \frac{\langle \sigma_{ij} \rangle_1}{(\epsilon_{11}^0)_1}, \quad i, j = 1, 2, 3 \quad (6)$$

The value of 0.001 is used as applied elastic strain in all effective elastic property load cases.

Effective thermal conductivities are determined by applying thermal gradients in the warp, weft, and binder directions. Similar to determining effective elastic properties, volume averaged heat flux  $\mathbf{q}$  is

extracted as follows:

$$\langle q_i \rangle_m = \frac{1}{V} \sum_{l=1}^{N_e} (q_i^{(l)})_m \cdot V^{(l)}, \quad i = 1, 2, 3 \quad (7)$$

where  $\langle q_i \rangle_m$  is the volume averaged heat flux from the  $m$ -th load case. Components of the homogenized thermal conductivity matrix are then also found similar to the effective stiffness. For example, from the first load case (applied gradient in the warp direction), components  $k_{i1}$  can be calculated:

$$k_{i1} = \frac{-\langle q_i \rangle_1}{\nabla T_1^0}, \quad i = 1, 2, 3 \quad (8)$$

where  $\nabla T_1^0$  is the only non-zero component of the prescribed temperature gradient vector in the first load case. The applied temperature gradient corresponding to 1 degree difference between opposite sides of the unit cell is used in the effective thermal conductivity load cases.

## 4. Results and discussions

### 4.1. Effect of small oscillations in material orientations

The overall elastic and thermal conductivity properties of the  $\mu$ CT-based models, along with the experimental results [21] are presented in Table 3. Initial FEA results from ‘‘Original  $\mu$ CT-Co’’ geometry are 20% and 32% less stiff in the warp and weft directions respectively compared to the averaged experimental results. Investigation into the source of the discrepancy in the stiffness revealed that the generated centerlines used to assign local material orientations exhibit high frequency waviness, see Fig. 8. This waviness is not expected in the actual specimens (and is not observed in the  $\mu$ CT data) due to pre-tensioning of the tows during weaving.

To more closely approximate the expected shape of the tow, the centerline points were smoothed via running average (with six points) thus decreasing the average directional change between centerline points, see Table 4. To determine directional change, two consecutive

Table 2  
Properties of carbon fiber and 12 K-tow with 80% volume fraction of the fibers.

Material	$E_1$ (GPa)	$E_2$ (GPa)	$G_{12}$ (GPa)	$k_1$ ( $\frac{W}{m \cdot K}$ )	$k_2$ ( $\frac{W}{m \cdot K}$ )	$\nu_{12}$	$\nu_{23}$
IM7 carbon fiber	276	23.1	27.6	5.40	1.08	0.350	0.300
RTM6 epoxy + IM7 carbon fibers	221	13.18	7.17	4.36	0.71	0.350	0.350

**Table 3**  
Overall elastic and thermal conductivity properties of the conformal  $\mu$ CT-based models.

	Original $\mu$ CT-Co	Avg $\mu$ CT-Co	Experimental results [21]
$E_1$ (warp), GPa	61.7	72.4	77.3
$E_2$ (weft), GPa	44.8	61.1	65.8
$E_3$ (binder), GPa	11.3	11.7	
$k_1$ (warp), $\frac{W}{m \cdot K}$	1.71	1.74	
$k_2$ (weft), $\frac{W}{m \cdot K}$	1.49	1.55	
$k_3$ (binder), $\frac{W}{m \cdot K}$	0.587	0.598	
$\nu_{12}$	0.071	0.059	
$\nu_{23}$	0.231	0.339	
$\nu_{13}$	0.276	0.402	
$G_{12}$ , GPa	4.55	4.31	
$G_{23}$ , GPa	2.87	2.87	
$G_{13}$ , GPa	2.94	2.90	

vectors were constructed using three consecutive centerline points. The angle between each pair of vectors was then evaluated using the dot product. A greater angle between each vector pair indicated a greater change in local centerline direction. Thus, the “Original  $\mu$ CT-Co” and “Avg  $\mu$ CT-Co” models are identical in all respects except the local material orientations in the tows. With smoother tow centerlines, the FEA results more closely approximate the average moduli obtained experimentally – the “Avg  $\mu$ CT-Co” results are only 6% and 7% less stiff in the warp and weft directions respectively. Material orientations can also be seen to have an effect on Poisson’s ratios where ratio  $\nu_{12}$  decreases by 17%,  $\nu_{23}$  and  $\nu_{13}$  both show an increase of 31%. Potential remaining sources of the difference between numerical predictions and experimental results include presence of artificial gaps between tows in the conformal FEA model, geometric variations between unit cells within the composite, variations in fiber volume fractions within tows and constituent material property variations. The following sections will reference the “Avg  $\mu$ CT-Co” results when making comparisons.

While centerline waviness significantly reduced effective elastic properties, the thermal properties were not as impacted (Table 3). In the warp and weft directions, the “Avg  $\mu$ CT-Co” thermal conductivity is greater than the “Original  $\mu$ CT-Co” thermal conductivity by only 1.7% and 3.9% respectively. The lower difference in the thermal conductivity compared to the stiffness implies thermal conductivity properties are not as sensitive to local material orientations.

#### 4.2. Comparison of overall thermo-elastic responses of DFMA- and $\mu$ CT-based unit cells

Results for the “DFMA-1” model show a lower Young’s modulus in the warp direction at 57.4 GPa compared to 67.7 GPa in the weft direction, see Table 5. Experimentally, average Young’s modulus in the warp direction is higher than the modulus in the weft direction, 77.3 GPa vs 65.8 GPa, respectively. This motivated investigation into the effect of volume fraction on the effective elastic properties. The

**Table 4**  
Statistics of the angle difference between consecutive segments in tow centerlines.

	Mean angle difference			Standard deviation of angle difference		
	DFMA-2 ( $\theta^\circ$ )	Raw $\mu$ CT-Co ( $\theta^\circ$ )	Avg $\mu$ CT-Co ( $\theta^\circ$ )	DFMA-2 ( $\theta^\circ$ )	Raw $\mu$ CT-Co ( $\theta^\circ$ )	Avg $\mu$ CT-Co ( $\theta^\circ$ )
Warp	2.82	14.3	2.64	2.30	10.8	3.73
Weft	2.82	9.24	1.61	2.28	9.23	2.46
Binder	2.86	18.0	4.78	2.30	14.2	3.71

**Table 5**  
Overall elastic and thermal conductivity properties of the DFMA- and  $\mu$ CT-based models.

	DFMA-1	DFMA-2	Avg $\mu$ CT-Co	Experimental results [21]
$E_1$ (warp), GPa	57.4	60.7	72.4	77.3
$E_2$ (weft), GPa	67.7	53.6	61.1	65.8
$E_3$ (binder), GPa	11.7	10.3	11.7	
$k_1$ (warp), $\frac{W}{m \cdot K}$	1.55	1.70	1.74	
$k_2$ (weft), $\frac{W}{m \cdot K}$	1.73	1.47	1.55	
$k_3$ (binder), $\frac{W}{m \cdot K}$	0.612	0.572	0.598	
$\nu_{12}$	0.047	0.059	0.059	
$\nu_{23}$	0.403	0.420	0.339	
$\nu_{13}$	0.417	0.451	0.402	
$G_{12}$ , GPa	4.36	4.18	4.31	
$G_{23}$ , GPa	2.97	2.84	2.87	
$G_{13}$ , GPa	3.10	2.93	2.90	

“DFMA-1” model has a higher volume fraction in the weft direction than the warp direction, as presented in Table 1. To further investigate the effect, a second DFMA model is created as discussed in Section 2.1.

The volume fractions of the “DFMA-2” model match the trend of the “Avg  $\mu$ CT-Co” model by having a higher volume fraction in the warp direction than the weft direction. The same trend is observed in the Young’s moduli – the modulus in the warp direction predicted at 60.7 GPa is now higher than the predicted value of 53.8 GPa in the weft direction. However, both values are lower than the “Avg  $\mu$ CT-Co” predictions and experimentally measured results. In particular, “DFMA-2” warp volume fraction is equal to “Avg  $\mu$ CT-Co” warp volume fraction though the Young’s modulus for the “DFMA-2” model is 16% lower than the “Avg  $\mu$ CT-Co” model in the same direction. Similarly, the “DFMA-2” weft volume fraction is 2.2% lower than the “Avg  $\mu$ CT-Co” weft volume fraction with a 12% lower Young’s modulus. Good correspondence between “DFMA-2” and “Avg  $\mu$ CT-Co” is observed for all three shear moduli and Poisson’s ratio  $\nu_{12}$ . The other two Poisson’s ratios,  $\nu_{23}$  and  $\nu_{13}$ , are overestimated by the “DFMA-2” model. Upon detailed inspection, the geometry of the DFMA-based warp tows exhibit pinching that is not present in the  $\mu$ CT-based geometry, see Fig. 6. Due to the warp tows being pre-tensioned in the manufacturing process, excessive pinching is not expected.

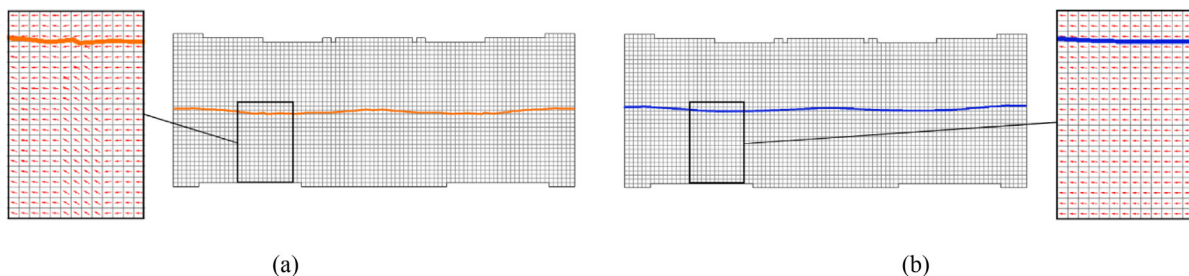


**Fig. 8.** Comparison of local material orientations in voxel representation of a weft tow: (a) before averaging; (b) after averaging. Orange and blue continuous lines represent centerlines of the tow before and after averaging, correspondingly.

Thermal conductivities in the warp and weft directions predicted by the “DFMA-2” model are 2.2% and 5.2% lower than the “Avg  $\mu$ CT-Co” model results, respectively. This small difference is consistent with the small difference in the models’ volume fractions. Thus, thermal conductivity is less sensitive to the tow shape and material orientations than the effective elastic response discussed above. This is true even considering the lower ratio of effective tow conductivities  $k_1/k_2$  compared to the higher ratio of effective tow Young’s moduli  $E_1/E_2$ .

#### 4.3. Voxel vs conformal meshes for prediction of effective properties

As previously discussed, a voxel mesh can more easily be generated from segmented  $\mu$ CT-based data and does not require the same amount of manual mesh preparation compared with conformal meshes. It is of interest to the authors whether a voxel mesh could predict similar overall thermo-elastic properties as a conformal mesh. Three different resolutions are used to investigate the sensitivity of predicted elastic and thermal conductivity properties to mesh resolution. A coarse fidelity mesh, “ $\mu$ CT-VX\_75” (662,700 elements, 685,902 nodes), a medium fidelity mesh, “ $\mu$ CT-VX\_100” (1,587,600 elements, 1,629,031 nodes), and a high fidelity mesh, “ $\mu$ CT-VX\_125” (3,120,500 elements, 3,185,408 nodes) were generated. The number at the end of each mesh name corresponds to the number of elements in the through thickness direction.

Based on the results presented in Table 6, there is very little difference in the moduli between the three voxel models’ predictions with the exception of  $E_2$ ,  $k_2$  and shear moduli. As the resolution increases, so do  $E_2$  and  $k_2$  while the shear moduli decrease. This can be explained by the increasing volume fraction of weft tows with resolution, see Table 1. Comparing the medium resolution model’s with the conformal model’s predictions, all Young’s moduli, shear modulus  $G_{12}$  and effective conductivities are within 3% of the “Avg  $\mu$ CT-Co” results. Shear moduli  $G_{23}$  and  $G_{13}$  are underpredicted by the medium resolution model by 6.6% and 5.9% respectively. High resolution model offers little improvement over the medium resolution model in terms of predictions for Young’s moduli and effective conductivities – they are within 2.5% of the conformal model results. Predictions for  $G_{23}$  and  $G_{13}$  are improved with increased number of voxels – they are underpredicted by only 3.8% and 3.1%, respectively, as compared with the conformal model. Voxel resolution has almost no effect on the Poisson’s ratios as they remain relatively constant between all voxel meshes and match the “Avg  $\mu$ CT-Co” model’s predictions; the maximum relative difference of 3.5% is observed for  $\nu_{12}$ .

These results indicate that a sufficiently detailed structured mesh, which can be more easily developed from the segmented microtomography data, can be a good substitute for a conformal mesh for estimating the overall thermo-elastic properties of 3D woven composites. It is worth pointing out, however, that medium and high

resolution voxel models have greater numbers of degrees of freedom compared to the conformal model. Therefore, each load case requires more time to run. As an illustration, a single uniaxial tension load case takes 3 min to run for  $\mu$ CT conformal model, and 7 and 16 min to run for medium and high resolution voxel models on an office computer with a single Intel i7-8700 processor and 32 GB memory. Nevertheless, even with increased simulation runtimes voxel models may still result in significant time savings given relative ease of model preparation requiring minimal user intervention following  $\mu$ CT data segmentation.

## 5. Conclusions

Two mesh generation techniques for meso-scale FEA of orthogonal 3D woven composites are evaluated by comparing FEA predictions of the overall Young’s moduli to experimental results. The techniques are: numerical simulation of fabric weaving using DFMA and direct processing of  $\mu$ CT data. For further comparison of the models, predictions for thermal conductivity are also considered. Tow shapes, local material orientations, and volume fractions vary between the models and have different effects on the predicted properties. The method for creating the  $\mu$ CT-based model is demonstrated to be robust enough to allow for the implementation of periodic boundary conditions. In addition, predictions from  $\mu$ CT-based voxel meshes having different resolutions are compared to the conformal mesh predictions. The architecture used for each model is a 1x1 orthogonal woven unit cell made from IM7 carbon fibers and RTM6 epoxy matrix.

Two realizations of the architecture were generated using DFMA software – naïve and  $\mu$ CT-informed. It is shown that the second realization, in which volume fractions of the warp, weft and binder tow groups were attempted to match  $\mu$ CT observations, performs better than the naïve realization in terms of predictions of effective Young’s moduli. However, both DFMA-based models performed worse than the model with geometry obtained directly from  $\mu$ CT data. Given similar volume fractions of the warp, weft and binder tow groups, the same material properties and boundary conditions, it appears that the primary source of the difference between the generated and imaging-based models is the shape of individual tows.

It is shown that accurate representation of the microstructure geometry is important for accurate prediction of the overall mechanical properties. In particular, high frequency oscillations in tow element orientations (a potential artifact of microtomography image processing) significantly reduce predicted stiffness in the warp and weft directions. In contrast, the oscillating material orientations do not affect predicted shear moduli and have little effect on the overall thermal conductivity. With averaged centerlines, the “Avg  $\mu$ CT-Co” model’s warp and weft elastic property predictions show good correspondence with the experimental results. It is also shown that tow volume fractions have a greater effect on thermal conductivity compared to local material

**Table 6**  
Overall elastic and thermal conductivity properties of the conformal and voxel  $\mu$ CT-based models.

	$\mu$ CT-VX_75	$\mu$ CT-VX_100	$\mu$ CT-VX_125	Avg $\mu$ CT-Co	Experimental results [21]
$E_1$ (warp), GPa	71.4	71.4	70.9	72.4	77.3
$E_2$ (weft), GPa	57.2	59.4	59.6	61.1	65.8
$E_3$ (binder), GPa	11.8	11.8	11.7	11.7	
$k_1$ (warp), $\frac{W}{m \cdot K}$	1.73	1.73	1.73	1.74	
$k_2$ (weft), $\frac{W}{m \cdot K}$	1.50	1.53	1.54	1.55	
$k_3$ (binder), $\frac{W}{m \cdot K}$	0.602	0.604	0.600	0.598	
$\nu_{12}$	0.059	0.057	0.057	0.059	
$\nu_{23}$	0.333	0.332	0.334	0.339	
$\nu_{13}$	0.397	0.398	0.399	0.402	
$G_{12}$ , GPa	4.40	4.38	4.34	4.31	
$G_{23}$ , GPa	3.11	3.06	2.98	2.87	
$G_{13}$ , GPa	3.13	3.07	2.99	2.90	

orientations.

Ability of voxel meshes to predict the effective thermo-elastic properties is studied. It is shown that the predictions from the medium resolution voxel mesh are in good correspondence with the conformal mesh results (most effective constants are within 3%). This conclusion indicates that the automated structured mesh approach for estimation of the effective thermo-elastic properties based on a segmented  $\mu$ CT data is a fast and accurate alternative to conformal mesh models which require significant user intervention and manual processing.

## 6. Data statement

The raw and processed data that support the findings of this study are available from the corresponding author, B. D., upon request.

## Declaration of Competing Interest

The authors declare that they have no known competing financial interests or personal relationships that could have appeared to influence the work reported in this paper.

## Acknowledgements

This material is based upon work supported by the National Science Foundation under Grant No. CMMI-1662098. The financial support of the New Mexico Space Grant Consortium through the NASA Cooperative Agreement NNX15AK41A is gratefully acknowledged.

## References

- [1] Huang T, Wang Y, Wang G. Review of the mechanical properties of a 3D woven composite and its applications. *Polym - Plast Technol Eng* 2018;57(8):740–56.
- [2] Hallal A, Younes R, Fardoun F. Review and comparative study of analytical modeling for the elastic properties of textile composites. *Compos Part B Eng* 2013;50:22–31.
- [3] Buchanan S, Grigorash A, Archer E, McIlhagger A, Quinn J, Stewart G. Analytical elastic stiffness model for 3D woven orthogonal interlock composites. *Compos Sci Technol* 2010;70(11):1597–604.
- [4] Lin H, Brown LP, Long AC. Modelling and simulating textile structures using TexGen. *Adv Mater Res* 2011;331:44–7.
- [5] Tsukrov I, et al. Finite element modeling to predict cure-induced microcracking in three-dimensional woven composites. *Int J Fract* 2011;172(2):209–16.
- [6] Doitrand A, Fagiano C, Irisarri F-X, Hirsekorn M. Comparison between voxel and consistent meso-scale models of woven composites. *Compos Part A Appl Sci Manuf* 2015;73:143–54.
- [7] Zhou G, Sun X, Wang Y. Multi-chain digital element analysis in textile mechanics. *Compos Sci Technol* 2004;64(2):239–44.
- [8] Huang L, Wang Y, Miao Y, Swenson D, Ma Y, Yen C-F. Dynamic relaxation approach with periodic boundary conditions in determining the 3-D woven textile micro-geometry. *Compos Struct* 2013;106:417–25.
- [9] Daelemans L, et al. Finite element simulation of the woven geometry and mechanical behaviour of a 3D woven dry fabric under tensile and shear loading using the digital element method. *Compos Sci Technol* 2016;137:177–87.
- [10] Garcea SC, Wang Y, Withers PJ. X-ray computed tomography of polymer composites. *Compos Sci Technol* 2018;156:305–19.
- [11] Ansar M, Xinwei W, Chouwei Z. Modeling strategies of 3D woven composites: a review. *Compos Struct* 2011;93(8):1947–63.
- [12] Lee CS, Chung SW, Shin H, Kim SJO. Virtual material characterization of 3D orthogonal woven composite materials by large-scale computing. *J Compos Mater* 2005;39(10):851–63.
- [13] Green SD, Matveev MY, Long AC, Ivanov D, Hallett SR. Mechanical modelling of 3D woven composites considering realistic unit cell geometry. *Compos Struct* 2014;118(1):284–93.
- [14] Liu Y, Straumit I, Vasiukov D, Lomov SV, Panier S. Prediction of linear and non-linear behavior of 3D woven composite using mesoscopic voxel models reconstructed from X-ray micro-tomography. *Compos Struct* 2017;179:568–79.
- [15] Joglekar S, Pankow M. Modeling of 3D woven composites using the digital element approach for accurate prediction of kinking under compressive loads. *Compos Struct* 2017;160:547–59.
- [16] Timoshchuk NV, Kasper KD, Bayraktar HH. Assessment of process-induced microcracks in 3D woven composites using meso-scale model simulations. *IOP Conf Ser Mater Sci Eng* 2018;406(1).
- [17] Drach B, Tsukrov I, Trofimov A, Gross T, Drach A. Comparison of stress-based failure criteria for prediction of curing induced damage in 3D woven composites. *Compos Struct* 2018;189:366–77.
- [18] El-Hage Y, Hind S, Robitaille F. Thermal conductivity of textile reinforcements for composites. *J Text Fibrous Mater* 2018.
- [19] K. Sharp, A. E. Bogdanovich, and N. Carolina, “High Through-Thickness Thermal Conductivity Composites Based on Three-Dimensional Woven Fiber Architectures,” vol. 46, no. 11, 2008.
- [20] J. Schuster, D. Heider, K. Sharp, and M. Glowania, “Thermal conductivities of three-dimensionally woven fabric composites,” vol. 68, pp. 2085–2091, 2008.
- [21] Vyshenska K. Thesis: numerical and experimental studies of mechanical behavior and cure induced stresses in 3d carbon/epoxy composites. University of New Hampshire; 2014.
- [22] Isart N, El Said B, Ivanov DS, Hallett SR, Mayugo JA, Blanco N. Internal geometric modelling of 3D woven composites: a comparison between different approaches. *Compos Struct* 2015;132:1219–30.
- [23] Drach A, Drach B, Tsukrov I. Processing of fiber architecture data for finite element modeling of 3D woven composites Dedicated to Professor Zdeněk Bittnar in occasion of his 70th birthday. *Adv Eng Softw* 2014;72:18–27.
- [24] Vasylevskiy K, Tsukrov I, Drach B, Buntrock H, Gross T. Identification of process-induced residual stresses in 3D woven carbon/epoxy composites by combination of FEA and blind hole drilling. *Compos Part A Appl Sci Manuf* 2020;130:105734.
- [25] Schneider CA, Rasband WS, Eliceiri KW. NIH Image to ImageJ: 25 years of image analysis. *Nat Methods* 2012;9(7):671–5.
- [26] L. Piegel and W. Tiller, *The NURBS Book*, 2nd editio. Berlin, Heidelberg: Springer Berlin Heidelberg, 1997.
- [27] “Rhinoceros 6.” Robert McNeel & Associates, Seattle, WA, USA.
- [28] “MSC Marc Mentat 2016.0.0.” MSC Software, Santa Ana, CA, USA.
- [29] “https://www.hexcel.com/user\_area/content\_media/raw/HexFlowRTM6DataSheetPDF.pdf,” Hexcel Corp. Accessed 20 Novemb. 2018.
- [30] M. Villière, D. Lecoite, V. Sobotka, N. Boyard, and D. Delaunay, “Composites : Part A Experimental determination and modeling of thermal conductivity tensor of carbon / epoxy composite,” vol. 46, pp. 60–68, 2013.
- [31] Hashin Z. Analysis of properties of fiber composites with anisotropic constituents. *J Appl Mech* 1979;46(3):543.
- [32] I. Tsukrov, M. Giovinazzo, K. Vyshenska, H. Bayraktar, J. Goering, and T. S. Gross, “Comparison of two approaches to model cure-induced microcracking in three-dimensional woven composites,” In: Proceedings of the 2012 International Mechanical Engineering Congress & Exposition (IMECE2012), 2012, pp. 1–6.
- [33] “https://www.hexcel.com/user\_area/content\_media/raw/IM7\_HexTow\_DataSheet.pdf,” Hexcel Corporation, Accessed: 20 November 2018. [https://www.hexcel.com/user\\_area/content\\_media/raw/IM7\\_HexTow\\_DataSheet.pdf](https://www.hexcel.com/user_area/content_media/raw/IM7_HexTow_DataSheet.pdf).
- [34] Drach B, Tsukrov I, Trofimov A. Comparison of full field and single pore approaches to homogenization of linearly elastic materials with pores of regular and irregular shapes. *Int J Solids Struct* 2016;96. <https://doi.org/10.1016/j.ijsolstr.2016.06.023>.